August. 2023

Micro-Macro Finite Element Modeling Method for Rub Response in Abradable Coating Materials

Jiahao Cheng[a], Xiaohua Hu[a*], William Joost[b], Xin Sun[a]

[a] Oak Ridge National Laboratory, Oak Ridge, TN 37831, United States

[b] Formerly Materials and Processes Engineering, Pratt & Whitney, East Hartford, CT, 06118, United States

*Corresponding author

E-mail address: hux3@ornl.gov

Abstract

Gas turbine engines experience "rub" when the rotating blades come in contact with a static abradable coating. This results in extreme strain rates and dynamics inside a high temperature/high pressure environment. Current rub models are phenomenological and do not reflect the underlying microstructures, thus limiting their prediction accuracy. In this work, a microstructure-informed, reduced order modeling framework is introduced for simulating abradable coating 'rub' behavior. This framework comprises a microscale model constructed based on digitized abradable microstructure and explicitly simulates the mechanical behavior of each constituent phases and their interactions. After calibration and validation with experiment data, the calibrated microscale model is used to generate data across a vast range of applied strain rates and temperature with various load paths. Then, the virtually generated data are used to fit the macroscopic reduced order model, which enables fast component-scale rub simulation without compromising the integrity of the complex material behavior. The proposed effort will address the technical challenge of predicting abradable material behavior during rub through the application of multiscale modeling from microstructure to engines behavior, effectively reducing the development costs and time of new abradable material for better "rub" properties.

Keywords: abradable coating material; microstructure; finite element modeling; reduced order model

1, Introduction

In contemporary gas turbine engines, abradable seal coatings are applied to casings/shrouds' inner surface to control tight clearances between the rotating blades and the static housing, thus maintaining high pressure and high temperature within the combustor and increasing engine efficiency. As the engine approaches peak power, thermal expansion and centrifugal forces induce blade extension, leading the blade tips to "rub" against the abradable material, crafting a cutting path similar to a machine tool process. The 'rub' between the blade and coating is characterized by extreme strain rate dynamics within the turbine's high temperature environment and put highly demanding requirements on abradable coating materials such as high-temperature resistance, impact resistance, low wear rate, not causing blade or tip wear, and etc. The choice of abradable coating materials mainly depends on the in-service temperature level and the blade material of the specific turbine model. For the low and intermediate pressure compressor which operates at temperatures of up to 618K, the Aluminum Silicon Polyester (AlSi-PES) abradable is commonly used in conjunction with Ti-6Al-4V blades. The AlSi-PES coating is produced by thermal spray and applied to the housing, resulting in a multiphase composite structure as illustrated in Fig. 1. Notably, this microstructure leads to loading path dependent material properties (Cheng et al., 2022; Pellegrino et al., 2018). Characterizing abradable based solely on hardness has proven insufficient (Lye et al., 2022), underlining the need for a comprehensive understanding of their constitutive behavior, especially in the context of flight cycle variations.

Due to the challenging and costly nature of direct measurements of 'rub' process during service, industries often resort to numerical models and validations to accelerate the advancement of abradable coating materials. The modeling efforts in this area mainly focus on two aspects: the 'rub' interaction and the microstructure-properties relationship. A large amount of research efforts have been placed on modeling the blade-casing interaction during turbine operation. Due to computation cost limitation, the works in this category are usually based on reduced order finite element models to simulate the dynamic of the rotor, casing, blade and liner system, and model the contact between blade and abradable using homogenized plasticity and removal/wear constitutive laws (Almeida et al., 2015; Berthoul et al., 2018; Legrand & Pierre, 2009; Williams, 2011). Other interaction models are based on analytical methods, such as component mode synthesis (CMS) method (Batailly et al., 2012; Nyssen & Batailly, 2019), and models based on delay differential equations for abradable liners removal and blade dynamics analysis (Olgac et al., 2014; Salvat et al., 2013).

While the above 'rub' interaction models provide predictability at the component level, they are based on homogenized plasticity and wear constitutive laws that do not reflect the underlying microstructure and do not capture the complex deformation behavior related to the fluctuation in applied temperature and strain rates. The limited macroscopic constitutive model results in conservative designs that bound efficiency and incur extensive testing requirements for certification. From a microstructural perspective, the relationship between abradable material composition and its physical and mechanical behavior remains a critical research avenue. The modeling effort in this direction attempted to bridge the gap between microstructural attributes and the resultant macroscopic behavior. Preliminary studies have focused on model thermal and elastic properties based on microstructure (Bakker, 1997; Bolot et al., 2011, 2017; Duramou et al., 2014; Faraoun et al., 2006; Jadhav et al., 2006; Kulkarni et al., 2003; Michlik & Berndt, 2006; Wang et al., 2003). Subsequent work addressed the complex tribological behavior of AlSi-PES abradables at microscale as developed in (Ribesse et al., 2014). Rate dependent plasticity constitutive laws spanning a wide range of temperature and strain rate range were proposed based on Split-Hopkinson Pressure Bar (SHPB) test results for the AlSi-PES abradables in (Skiba et al., 2020, 2021). Very recently, a three-dimensional x-ray computed tomography (xCT) reconstructed microstructural finite element model is developed with the temperature and rate dependent plasticity and damage laws for each constituent phase agreements (Cheng et al., 2022). The model was validated against tensile and compressive experiments at room and elevated temperature, showing good. Neural networks (NNs) based approach was also developed to inversely determine the properties of the individual phases of abradables in (Lye et al., 2022), providing an alternative route for constitutive behavior modeling. The above explicit microstructure-properties models can provide guidance in improving the mechanical performance of the reinforced polymer composites by optimizing the volume fraction and/or the geometrical features, similar to improving the buckling strength of thin-wall carbon nanotube (CNT)/ polylactic acid(PLA)/carbon fiber(CF) composite (Cao, 2023a), the bending and shear strength of PLA- glass fiber reinforced composite (Cao et al., 2023) and toughness of CF-reinforced thermoplastic composites(Cao, 2023b).

Nonetheless, the aerospace and energy industries have highlighted the need for sophisticated and integrated numerical models that encapsulate the complex plasticity and failure behavior into the component scale blade-casing dynamic rub simulations. In this paper, we propose a micro-macro modeling framework designated to translate the underlying microstructure behavior to macroscopic performance and 'rub' simulation. The framework's schematic is shown in Fig.2. The framework composes of a microscopic Representative Volume Element (Micro-RVE) model that explicitly capture the influence of microstructure to the deformation and failure behavior, adopted from authors' previous work (Cheng et al., 2022). The novelty of this work is proposing a macroscopic reduced order constitutive model (macro-ROM) for the component scale "rub" simulation. The macro-ROM is developed using the virtually generated stress-strain data obtained by running micro-RVE simulations under various applied strain modes, temperature and strain rates. The macro-ROM captures the same complex plasticity and damage behavior as the micro-RVE model, including tension-compression asymmetry and strong temperature and strain rate sensitivities, with target for efficient component scale simulation and addressing the locally varying loading path, temperature and rate conditions. The proposed micro-macro modeling approach enables microstructure-informed, more precise predictions and facilitating the evolution of next-generation abradable materials.

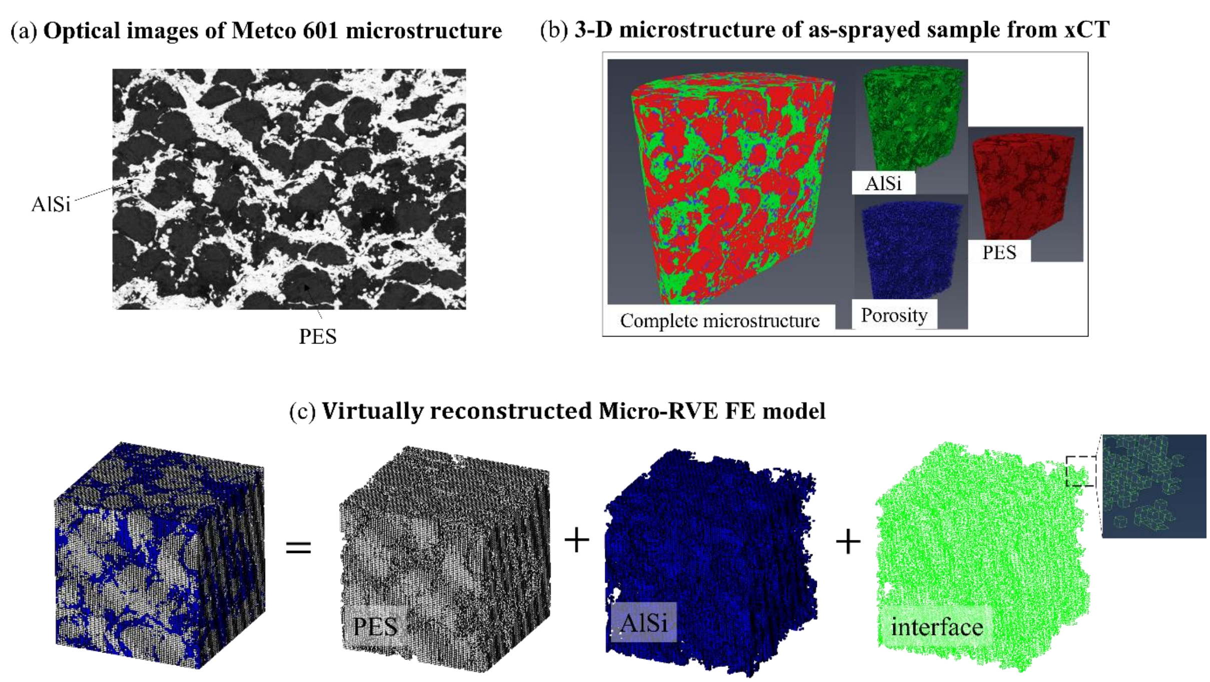

Figure 1. Microstructure characterization and micro-RVE model of AlSi-PES Metco601 (Cheng et al., 2022). (a) Optical images of AlSi-PES Metco 601 microstructure at 200x resolution. (b) three-dimensional (3-D) Metco601 microstructure obtained from xCT characterization. (c) the virtually reconstructed finite element (FE) model based on xCT for micro-RVE simulation. The measured volume fractions of the AlSi, PES and porosity are 34.70 vol.%, 55.23 vol.%, and 10.07 vol.%, respectively, which are statistically converged to xCT.

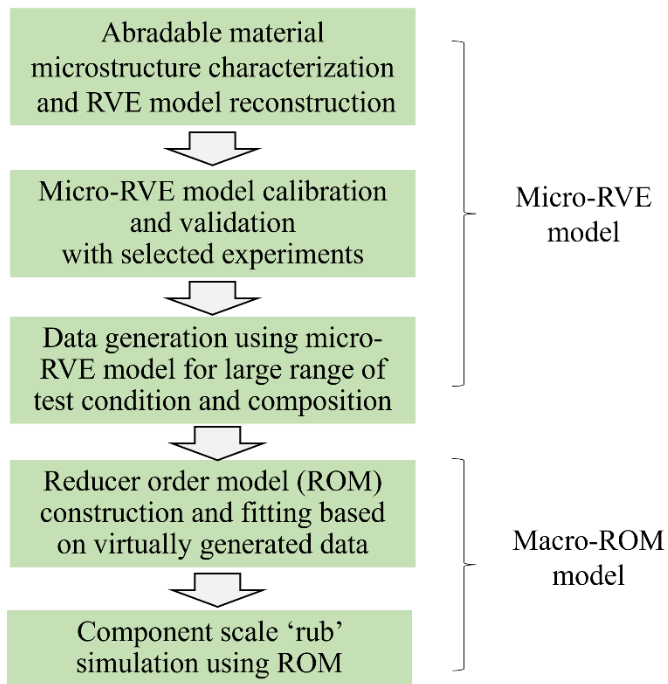

Figure 2. The schematic of micro-macro modeling framework.

2, Microscopic Representative Volume Element (Micro-RVE) model

The research work in this paper focuses on Metco 601, an AlSi-PES abradable coating material (Fig. 1) for low and intermediate pressure compressor. The micro-RVE model was proposed by authors in (Cheng et al., 2022) and is summarized in this section for the completeness of the paper. The microstructure of Metco 601 comprises AlSi matrix, PES dislocator and porosities. Using xCT, the micro-RVE model of the Metco 601 was reconstructed with eight-node reduced-integration linear brick elements (C3D8RT) in voxelized mesh. The porosities were created by removing elements from the FE mesh at corresponding locations found in the actual xCT microstructure. The final RVE model is $1mm \times 1mm \times 1mm$, which is sufficiently large for statistical convergence on the volume fractions of each phase. The commercial finite element package ABAQUS/Explicit is used for micro-RVE simulation, where the model was implemented by writing user-defined subroutines.

2.1 Constitutive model for AlSi phase

The Johnson-Cook plasticity model, typically used for cast aluminum alloys, was employed for describing the temperature and strain rate-dependence of the yield stress, which is expressed as:

$$\sigma^{Y} = \left(A + B\varepsilon_p^n\right)\left(1 + C\ln\frac{\dot{\varepsilon}_p}{\dot{\varepsilon}_0}\right)\left(1 - \left(\frac{\theta - \theta_{ref}}{\theta_{melt}^{AlSi} - \theta_{ref}}\right)^m\right) \tag{1}$$

Here, ε_p and $\dot{\varepsilon}_p$ are the equivalent plastic strain and its rate, $\dot{\varepsilon}_0 = 1\ s^{-1}$ is a constant for reference rate. θ is the applied temperature, $\theta_{ref} = 298K$ is the reference temperature and $\theta_{melt}^{AlSi} = 850\mathrm{K}$ is the melting temperature of AlSi phase (Kotzé et al., 2013). *A*, *B*, *C* are calibratable material parameters for initial yield stress, strain hardening rate and strain rate dependence, respectively. *m* and *n* are calibratable exponent parameters controlling temperature and strain rate sensitivity, respectively.

The failure of the AlSi phase was captured in the FE model using a Rice-Tracey damage law (Rice & Tracey, 1971), which is written as:

$$\varepsilon^{crit} = d_1^{AlSi}\exp\left(-d_2^{AlSi}\frac{p}{\sigma_{VM}}\right)\left(1 + d_3^{AlSi}\log\left(\frac{\dot{\varepsilon}}{\dot{\varepsilon}_0}\right)\right)\left(1 + d_4^{AlSi}\theta^*\right) \tag{2}$$

where ε^{crit} is the critical plastic strain for failure initiation. p is hydrostatic pressure, σ_{VM} is the von Mises stress. $\dot{\varepsilon}$ is the applied strain rate. $d_{1\ldots4}^{AlSi}$ are calibratable material parameters, and d_2^{AlSi}, d_3^{AlSi} and d_4^{AlSi}accounts for the sensitivity to stress-triaxiality, strain rate and temperature. Once initiated, the damage at an element integration point increases linearly proportional to the dissipated energy due to plastic deformation, according to:

$$\dot{D}_{AlSi} = \begin{cases} \dfrac{\boldsymbol{\sigma} : \dot{\boldsymbol{D}}^p}{E^D} & if\ \varepsilon_p \geq \varepsilon^{crit} \\ 0 & if\ \varepsilon_p < \varepsilon^{crit} \end{cases} \tag{3}$$

where $\boldsymbol{\sigma}$ denotes the Cauchy stress, and $\dot{\boldsymbol{D}}^p$ is the plastic deformation rate tensor. $D_{AlSi} \in [0, D_{max}]$ is the damage parameter. The upper bound D_{max} is set to 0.99 to keep a small threshold strength for numerical stabilization, E^D is the reference dissipated energy per unit volume to define the damage evolution rate. The material strength degrades with damage evolution, according to:

$$dev(\boldsymbol{\sigma}) = (1 - D_{AlSi})\, dev(\hat{\boldsymbol{\sigma}}) \tag{4}$$

$$p = \left(1 - D_{AlSi}^{vol}\right)\hat{p}; \qquad D_{AlSi}^{vol} = \begin{cases} D_{AlSi} & if\ \hat{p} \leq 0 \\ 0 & if\ \hat{p} > 0 \end{cases} \tag{5}$$

where $dev(\boldsymbol{\sigma})$ and $p = \frac{1}{3}tr(\boldsymbol{\sigma})$ are the deviatoric and hydrostatic components of $\boldsymbol{\sigma}$, respectively. The symbol $\hat{}$ indicates the undamaged value. To introduce tension-compression asymmetry in failure behavior, the variable D_{AlSi}^{vol} is defined to ensure the volumetric components of stress remain unaffected when the material point is under compressive stress stage, and is only degraded when subjected to tensile stress. The shear or deviatoric component of stress is always degraded.

2.2 Constitutive model for PES phase

The PES experience sharp change in elastic and plastic response before and after the glass transition temperature θ_g, which is be described by a comprehensive constitutive model in (Richeton et al., 2007) and adopted in this work. The plastic flow rule of PES is expressed as

$$\dot{\gamma}_p = \begin{cases} \dot{\gamma}_0 \exp\left(-\dfrac{\Delta H_\beta}{k\theta}\right) \sinh^n\left(\dfrac{(\tau - \tau_{int})V}{2k\theta}\right) & if\ \theta \leq \theta_g \\ \dot{\gamma}_0 \exp\left(-\dfrac{\Delta H_\beta}{k\theta}\right) exp\left(\dfrac{\ln 10\, c_1^g(\theta - \theta_g)}{c_2^g + \theta - \theta_g}\right) \sinh^n\left(\dfrac{\tau V}{2k\theta}\right) & if\ \theta > \theta_g \end{cases} \tag{6}$$

where $\dot{\gamma}_p$is the plastic strain rate. $\dot{\gamma}_0$ is a reference factor. ΔH_β and V are the activation energy and shear activation volume, k is Boltzmann's constant. n is a material parameter describing the cooperative nature of the polymer chain segments. c_1^g and c_2^g are the William-Landel-Ferry (WLF) parameters relative to θ_g. $\tau = \left[\frac{1}{2}\overline{\boldsymbol{T}}^{dev}:\overline{\boldsymbol{T}}^{dev}\right]^{\frac{1}{2}}$ is the equivalent shear stress (see equation 14). τ_{int} is the shear resistance.

The PES usually goes through a material softening period upon initial plastic deformation due to the polymer molecular defects rearranging mechanism, leading to formation of shear bands. To describe the material softening, τ_{int} is expressed as:

$$\begin{aligned} &\text{Initial shear resistance:} \quad \tau_{int}(t=0) = \tau_{int}^{ref} - \widehat{m}\theta + \alpha_p P \\ &\text{shear resistance evolution:} \quad \dot{\tau}_{int} = h\left(1 - \frac{\tau_{int}}{\tau_{ps}}\right)\dot{\gamma}_p \end{aligned} \tag{7}$$

Where τ_{int}^{ref} is the reference internal shear stress at the absolute zero temperature $\theta = 0K$. $\widehat{m}$ and α_p are the fitting parameters for the temperature and pressure dependence. h is a hardening or softening slope parameter and τ_{ps} is the saturation state stress, which is assumed to have a fixed ratio to the τ_{int} at the initial stage ($time\ t = 0$) (Richeton et al., 2007).

After the initial softening, the further plastic deformation of PES induces a kinematic hardening due to the reorientation of polymer chains (Arruda & Boyce, 1993), which is described by a back stress tensor $\boldsymbol{B}$ in the model, expressed as:

$$\boldsymbol{B} = \sum_{i=1..3} B_i\, \boldsymbol{n}_i^p \otimes \boldsymbol{n}_i^p \ ; \quad B_i = C_R(\theta)\sqrt{\frac{N(\theta)}{3}}\mathcal{L}^{-1}\left(\frac{\lambda_{chain}}{\sqrt{N(\theta)}}\right)\frac{\lambda_i^2 - \lambda_{chain}^2}{\lambda_{chain}}, i = 1,2,3 \tag{8}$$

Where $B_{i=1..3}$ are the principal components of the back stress tensor $\boldsymbol{B}$, $\lambda_{i=1..3}$ and $\boldsymbol{n}_{i=1..3}^p$ are the eigen-values and eigen-vectors of the left plastic stretch tensor $\boldsymbol{V}^p$ (symmetric part of $\boldsymbol{F}^p$, see equation 11). $\lambda_{chain} = \frac{1}{\sqrt{3}}(\lambda_1^2 + \lambda_2^2 + \lambda_3^2)^{1/2}$. $\mathcal{L}^{-1}(x) \approx x(3 - x^2)/(1 - x^2)$ is the inverse Langevin function with Pade´ approximation. $C_R(\theta)$ is the rubbery modulus and $N(\theta)$ is the number of rigid chain links between entanglements. Note that when the glassy polymer is heated above θ_g, its polymer chains fully recover to the isotropic unoriented state. Therefore, the rubbery modulus $C_R(\theta)$ and rigid chain links number $N(\theta)$ are set to be piece-wise linear functions of temperature, respectively expressed as:

$$C_R(\theta) = \begin{cases} C_R(0) - a\theta & if\ \theta \le \theta_g \\ \dfrac{C_R(0) - a\theta_g}{\theta_g}\theta & if\ \theta > \theta_g \end{cases} \ ; \quad N(\theta) = \begin{cases} N(0) + b\theta & if\ \theta \le \theta_g \\ N(0) + b\theta_g & if\ \theta > \theta_g \end{cases} \tag{9}$$

To simulate large deformation and failure of AlSi-PES, the above flow equations and softening/hardening equations can be implemented in a finite deformation framework, which are summarized as the following:

$$\text{Kinematic equation:} \quad \boldsymbol{F} = \boldsymbol{F}^e \boldsymbol{F}^{th} \boldsymbol{F}^p \tag{10}$$

$$\text{Polar decomposition:} \quad \boldsymbol{F}^e = \boldsymbol{V}^e \boldsymbol{R}^e \tag{11}$$

$$\text{Velocity gradient decomposition:} \quad \begin{array}{c} \boldsymbol{L} = \dot{\boldsymbol{F}}\boldsymbol{F}^{-1} = \boldsymbol{L}^e + \boldsymbol{F}^e[\boldsymbol{L}^{th} + \bar{\boldsymbol{L}}^p]\boldsymbol{F}^{e^{-1}} \\ \boldsymbol{L}^e = \dot{\boldsymbol{F}}^e \boldsymbol{F}^{e^{-1}}, \boldsymbol{L}^{th} = \dot{\boldsymbol{F}}^{th} \boldsymbol{F}^{th^{-1}} = \beta^{poly}(\theta)\dot{\theta}\boldsymbol{I} \\ \boldsymbol{L}^p = \dot{\boldsymbol{F}}^p \boldsymbol{F}^{p^{-1}}, \bar{\boldsymbol{L}}^p = \boldsymbol{F}^{th}\boldsymbol{L}^p\boldsymbol{F}^{th^{-1}} \end{array} \tag{12}$$

$$\text{Flow rule equation:} \quad \bar{\boldsymbol{L}}^p = \dot{\gamma}_p \frac{(\bar{\boldsymbol{T}}^{dev})}{||\bar{\boldsymbol{T}}^{dev}||} \; ; \; \bar{\boldsymbol{T}} = \boldsymbol{R}^{e^T}\boldsymbol{T}\boldsymbol{R}^e - \boldsymbol{B} \tag{13}$$

$$\text{Stress} - \text{strain equations:} \quad \boldsymbol{T} = \frac{1}{\det(\boldsymbol{F})}\mathbb{C}^e \ln(\boldsymbol{V}^e) \tag{14}$$

where $\boldsymbol{F}, \boldsymbol{F}^e, \boldsymbol{F}^{th}$, and $\boldsymbol{F}^p$ are the total, elastic, thermal and plastic deformation gradient tensor, respectively. $\boldsymbol{V}^e$ and $\boldsymbol{R}^e$ are the left stretch tensor and rotation tensor, respectively. $\boldsymbol{L}$ is the velocity gradient tensor, which is decomposed into the elastic, thermal, and plastic parts ($\boldsymbol{L}^e$, $\boldsymbol{L}^{th}$ and $\boldsymbol{L}^p$). $\boldsymbol{T}$ is a finite deformation Cauchy stress tensor, and $\bar{\boldsymbol{T}} = \boldsymbol{R}^{e^T}\boldsymbol{T}\boldsymbol{R}^e - \boldsymbol{B}$ is the stress tensor by converting $\boldsymbol{T}$ to intermedium configuration and considering back stress **B.**

Under tensile stress, PES exhibits a transition from brittle failure to ductile failure as the temperature increases. At room temperature, the PES fails by formation of crazes which are oriented fibrillar bridge chains that act as stabilizers. The breakage of crazes requires stress concentration similar to brittle crack propagation. As temperature increases, the formation of crazes is gradually suppressed, and material fails by microvoids formation and coalescence. To account for the increase of ductility with temperature, the following damage model is proposed for PES phase (Cheng et al., 2022):

$$\sigma^{hy} \geq \sigma^{crit}_{poly} + (\theta - \theta_{ref})d^{hy}_{poly} \tag{15}$$

where σ^{hy} is the hydrostatic stress. σ_{poly}^{crit} is the critical stress for brittle failure at room temperature $\theta_{ref} = 298K$. d_{poly}^{hy} is a parameter describing the change of failure stress with temperature.

At last, the glass transition temperature (θ_g) of PES is also affected by the applied strain rate as higher strain rate increases the glass transition temperature (Richeton et al., 2005). The elastic modulus (E) of PES are also functions of the ambient temperature. The temperature dependence of θ_g and E needs to be considered in the model and are provided in details in (Cheng et al., 2022).

2.3 Constitutive model for AlSi-polyester interface

The polyester-AlSi interface and its debonding is modeled using three-dimensional eight node cohesive (COH3D8) elements with a bilinear traction-separation law in the micro-RVE model. The traction force at the interface increases linearly until reaching a critical separation, which is expressed as:

$$t_{n/s/t} = K_{n/s/t}\, \delta_{n/s/t}; \;\; \max\left\{\frac{<\delta_n>}{\delta_n^0}, \frac{\delta_s}{\delta_s^0}, \frac{\delta_t}{\delta_t^0}\right\} = 1 \tag{16}$$

where $t_{n/s/t}$ is the traction force in normal/shear/tangent directions, $K_{n/s/t}$ is the corresponding stiffness in the three directions, and the $\delta_{n/s/t}$ is the separation distance. $\delta_{n/s/t}^o$ represent the corresponding peak values of separation in the three directions. $< >$ are the Macaulay brackets. After failure imitation, the traction force reduces to zero with further amount of separation ($\delta_{n/s/t}^f - \delta_{n/s/t}^o$) and remains zero thereafter. The stiffness constants were assumed to follow the relation (Hesebeck, 2015):

$$K_n = \frac{E^{coh}}{t^{coh}}; \quad K_s = K_t = \frac{E^{coh}}{(1-\nu)t^{coh}} \tag{17}$$

where E^{coh} is the effective elastic modulus for a cohesive element, t^{coh}= 0.1μm is the assumed thickness of interface, and ν is the Poisson's ratio. Both PES and AlSi uses a Poisson's ratio of 0.35 in the model. For simplicity, it was further assumed $\delta_n^0 = \delta_s^0 = \delta_t^0$ and $\delta_n^f = \delta_s^f = \delta_t^f$.

The COH3D8 cohesive interface element will be removed from the simulation once it is completely debonded (separation reaching $\delta_{n/s/t}^f$). Then, the new surfaces are created on AlSi and

PES debonded region using the "internal surface" feature in ABAQUS/Explicit. Once debonded, "hard" contact condition between the two new surfaces is activated using the "general contact" feature in Abaqus in order to correctly capture the sliding and re-contact with each other during the subsequent deformation.

2.4 Calibration and validation of micro-RVE model

The model parameters for the micro-RVE model is calibrated by matching the high strain rate Split-Hopkinson Pressure Bar (SHPB) tests of Metco 601. The experiments were conducted at the Dynamic Mechanics of Materials Laboratory (DMML) of Ohio State University (OSU) (Cheng et al., 2022). Uniaxial compression and tension tests were conducted separately on the same batch of samples at two selected test temperatures 298K (room temperature) and 533K, the latter is close to the glass transition temperature of PES ($\theta_g \cong 545$K based on dilatometer measurement). The average applied strain rate for the uniaxial compression and tension tests was 2000 s^{-1} and 325 s^{-1} , respectively. In addition to our tests, dynamic SHPB experiments of the Metco601 were also conducted and reported in (Pellegrino et al., 2018) and also used as additional data for calibration.

The calibration results for RVE model are shown in Fig.3, and the parameters are listed in table 1. The detailed calibration process involves a non-trivial process executed in seven steps, which is depicted in (Cheng et al., 2022). Fig.3a shows the single-phase stress-strain curves up to material point of failure (FP) for both AlSi and PES phases, computed at a reference strain rate of $10^{-3}s^{-1}$ and at various temperatures. Strong difference in yield stress and strain-to-failure are observed between the two phases. The comparison between the simulation results and SHPB data are shown in Fig. 3b, where satisfactory matching is obtained for various tests. Fig. 3c plots the von Mises stress distribution in uniaxial compression and tension tests at room temperature, respectively. The failure modes at 533K are similar to the room temperature results but with higher deformation heterogeneity. In both tension and compression test cases, it is observed the stress localized in the AlSi matrix, due to its much higher stiffness and yield stress. We note that despite the calibrated AlSi yield and hardening stress (~400MPa at room temperature) is much higher than PES phase, it did not increase the yield and hardening stress of AlSi-PES composite by a tremendous amount. Aside from the lower volume fraction, the lack of strengthening effect can be also due to the interpenetrating dendritic structure of AlSi. In compression, this could be due to the interpenetrating dendritic structure of AlSi-PES composite leads to many AlSi branches and struts are going through bending deformation rather than uniaxial compression and did not significantly increase the compression resistance, which is similar to what is observed in interpenetrating metal-metal composites (Cheng et al., 2020). The rest load-bearing AlSi struts undergoes a large local strain before the occurrence of damage, and the continuous occurrence of damage in AlSi struts leads to gradual stress reduction after reaching the peak stress at ~7% strain. In tension, the composite failed prematurely due to interface debonding that occurred very early, resulting in a very strong tension-compression asymmetry as shown in Fig. 3b. Noted that the premature failure was also observed in the digital image correlation (DIC) results during the SHPB test, showing consistency with the simulation.

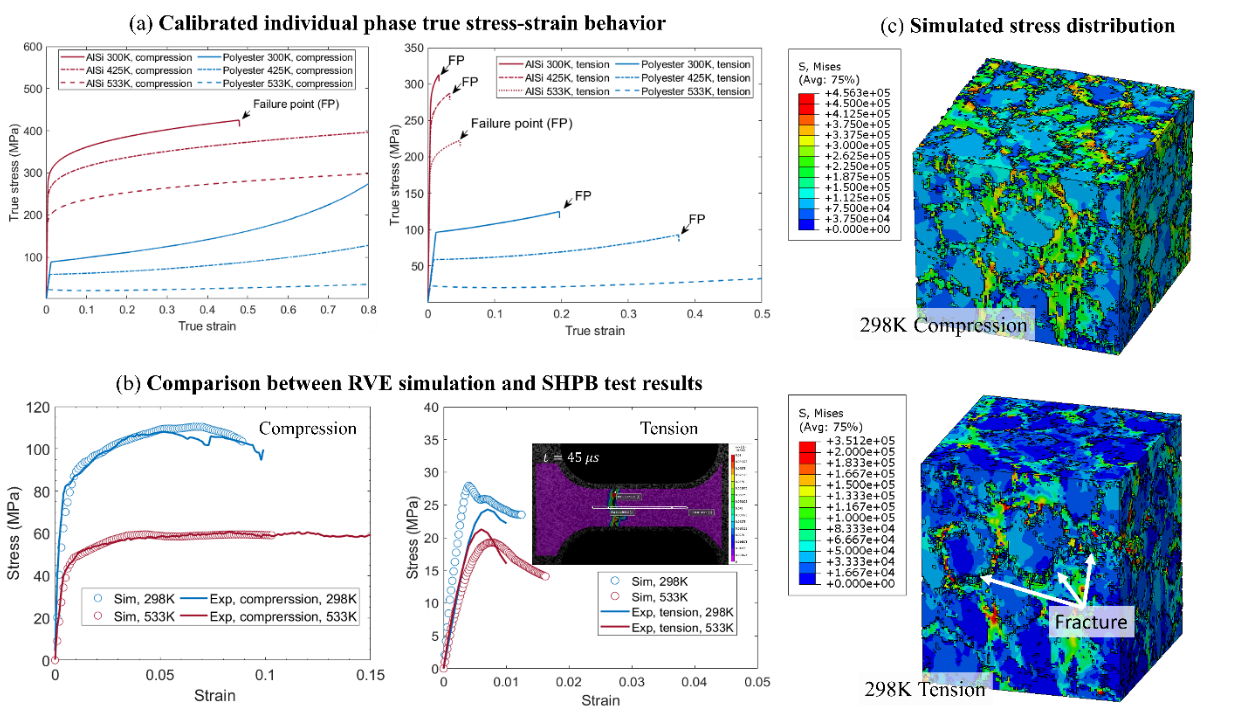

Figure 3. (a) The ‘true’ stress-strain behavior of AlSi and PES phase at different temperature, based on calibrated micro-RVE model parameters. (b) The comparison of simulated stress-strain behavior at 298K and 533K under tension at an applied strain rate of 2000 s^{-1}, and under compression at an applied strain rate of 325 s^{-1}, respectively. The subfigure in tension results plot shows the DIC image of premature localized fracture band formation during SHPB test. (c) the micro-RVE simulation predicted local von Mises stress distribution in compression and tension at 298K, respectively. The localized premature fracture is observed in tension due to AlSi-PES interface debonding.

3 Macroscopic reduced order model (Macro-ROM)

The reduced-order macroscopic constitutive model is formulated based on the volumetric homogenization of the stress-strain behavior obtained from microstructural simulation results, and target to apply for macroscopic scale (coupon and higher level) finite element simulation of 'rub' process. It is crucial for the reduced order model to capture the micro-RVE simulation predicted features including temperature sensitivity, strain rate sensitivity, tension-compression asymmetry in yield strength and ductility, etc. For this purpose, the following deformation and damage model is proposed.

The evolution of the plastic deformation for the homogenized ROM is described by an associated plastic flow rule:

$$\boldsymbol{L}^p = \dot{\boldsymbol{F}}^p \boldsymbol{F}^{p^{-1}} = \dot{d}_0 \left(\frac{\hat{\tau}}{g(\theta)}\right)^{\frac{1}{m}} \overline{\boldsymbol{N}} \tag{18}$$

where $\overline{\boldsymbol{N}} = \frac{\boldsymbol{\sigma}^{dev}}{\|\boldsymbol{\sigma}^{dev}\|}$ is the flow direction tensor, following the direction of deviatoric components of the Cauchy stress. $\dot{d}_0$ is a constant pre-factor, and m is the temperature dependent strain rate parameter simplified as a constant in this work. To introduce tension-compression asymmetry in yield and hardening stress, the effective flow stress, $\hat{\tau}$, is expressed as:

$$\hat{\tau} = [(|\lambda_1| - k\lambda_1)^a + (|\lambda_2| - k\lambda_2)^a + (|\lambda_3| - k\lambda_3)^a]^{\frac{1}{a}} \tag{19}$$

where $\lambda_1 - \lambda_3$ are the three eigenvalues of the deviatoric part of Cauchy stress ($\boldsymbol{\sigma}^{dev}$), k is a calibratable parameter that controls the tension-compression asymmetry, a is a constant that controls the smoothness of yield surface. $g(T)$ in equation (18) is the temperature dependent yield stress. The evolution of $g(T)$ is described by the following hardening law:

$$g(\theta) = g_0(\theta_0) + \alpha(\theta)\left[\exp\left(-\left(\frac{\varepsilon^p}{\beta(\theta)}\right)^{\psi}\right)\right] + H(\theta)\varepsilon^p \tag{20}$$

where the first term $g_0(\theta) = \hat{g}_0 - s_{g_0}\theta_0$ is the initial resistance that dependent on the initial temperature θ_0. $\alpha(\theta) = \hat{\alpha} - s_\alpha\theta$ is a temperature dependent pre-factor for non-linear hardening stress, and $\beta(\theta) = \hat{\beta} + s_\beta\theta$ is the temperature dependent non-linear hardening parameter. ψ is an constant exponent for non-linear hardening. $H(\theta) = \widehat{H} + s_H exp\left(-\frac{\theta}{\theta_{ref}}\right)$ is the pre-factor parameter as a function of temperature to describe the linear hardening rate. $\hat{g}_0$, $\hat{\alpha}$, $\hat{\beta}$, $\widehat{H}, s_{g_0}, s_\alpha, s_\beta, s_H$ are constants that fit the temperature dependence of the hardening behavior.

Finally, the tension-compression asymmetric material failure behavior of the homogenized model is described by the Johnson-Cook damage law, expressed as

$$\varepsilon_D^{ini} = \left[d_1^{ROM} + d_2^{ROM} \exp\left(-d_3^{ROM} \frac{p}{\sigma_{VM}}\right)\right]\left[1 + d_4^{ROM} \ln\left(\frac{\dot{\varepsilon}}{\dot{\varepsilon_0}}\right)\right][1 + d_5^{ROM}\theta] \tag{21}$$

where $d_1^{ROM} - d_5^{ROM}$ are fitting parameters accounts for the reference critical failure initiation strain, sensitivity to stress-triaxiality, strain rate and temperature, respectively. From the micro-RVE simulation and experiment results, the stress reduction slope, which is associated with the damage evolution rate, is also sensitive to the testing temperature and stress stage (described by stress triaxiality). Therefore, the following damage propagation model is introduced in ROM to account for the temperature and stress triaxiality dependence:

$$\dot{D}_{ROM} = \frac{\dot{\boldsymbol{D}}^p}{\varepsilon_D^{degrad}}$$
$$\varepsilon_D^{degrad} = \left[d_1^{degrad} + d_2^{degrad} exp\left(d_3^{degrad} \frac{p}{\sigma_{VM}}\right)\right] [1 + d_4^{degrad}\theta] \tag{22}$$

where $\dot{D}_{ROM}$is the damage evolution rate in the ROM model, ε_D^{degrad} is a variable controlling the damage evolution rate, $d_1^{degrad} - d_4^{degrad}$ are calibratable parameters. d_2^{degrad} and d_2^{degrad} controls the sensitivity to stress triaxiality, while d_4^{degrad} controls the sensitivity to applied temperature. Similar to the AlSi phase in micro-RVE model, the material strength degradation associated with damage evolution only applies for hydrostatic tension and shear stress components, while maintaining the stress for hydrostatic compression stress components, according to:

$$dev(\boldsymbol{\sigma}) = (1 - D_{ROM})\, dev(\widehat{\boldsymbol{\sigma}}) \tag{23}$$

$$p = \left(1 - D_{ROM}^{vol}\right)\hat{p}; \qquad D_{ROM}^{vol} = \begin{cases} D_{ROM} & if\ \hat{p} \leq 0 \\ 0 & if\ \hat{p} > 0 \end{cases} \tag{24}$$

where $dev(\boldsymbol{\sigma})$ and $p = \frac{1}{3}tr(\boldsymbol{\sigma})$ are the deviatoric and hydrostatic part of $\boldsymbol{\sigma}$ for ROM model, respectively.

The parameters of the reduced order model are fitted to match the data generated from microstructural finite element model simulations, thereby connecting the microstructure-informed complicated stress state, strain rate, and temperature dependent mechanical response to the continuum model suitable for macroscopic simulations. In particular, by homogenizing the microstructure simulations into a reduced order model we are able to quickly simulate abradable material removal process. For example, the microstructure REV of Metco 601 with total size of 0.5 mm by 0.5 mm by 0.5 mm requires approximately 6 hours to simulate 10% strain on 48 high performance computing cores, while the reduced order model obtains the same macroscopic stress-strain response in approximately 2 seconds on a single personal computer processor. The calibrated reduced order model thus enables the efficient and reliable of the limit rub simulation at a macroscopic structural scale.

To ensure the macroscopic model adequately replicates the micro-RVE model's homogenized response, the fitting data from micro-RVE model needs to cover testing conditions across a range of strain rates and temperatures that is relevant to the blade-Metco601 rubbing condition in engine. In this work, three strain rates ($\dot{\varepsilon} = 10^2, 10^3, 10^4$) and four different temperatures (300K, 400K, 500K, 550K) are selected for uniaxial compression and tension simulation, which yield a total number of 24 simulations. Note that even though this work only illustrate the modeling framework using tension or compression loading conditions, the data generation should ideally consider more complicated biaxial and triaxial loading condition, shear and other deformation modes for fitting a high confidence macro-ROM. This is subjected to future follow-up work.

The corresponding calibrated Reduced order model simulation results, obtained by applying the uniaxial tension/compression load on a single C3D8RT element at designated temperature and strain rate in ABAQUS/Explicit, are shown in Fig. 4. Satisfactory agreement between the reduced order model and micro-RVE model stress-strain curves are obtained in most test conditions except some mismatch during tension at 400K and 500K and applied strain rate of $10^2\ s^{-1}$. In general, the results supported the capability of the Macro-reduced order model.

In addition to current reduced order model formulation, it is noteworthy that the reduced order model can be also extended as a function of abradable compositions. For example, the micro-RVE model can be utilized to study the mechanical response of AlSi-PES abradables with varying volume fractions of each phase, as well as study the effect of controlling porosity fraction. Based on the new microstructures, the micro-RVE model simulations can be conducted to expand the generated dataset to include the microstructure variation. The current macro-ROM model parameters can be re-calibrated for each microstructure variation, then identify the parameters as a function of microstructure factors (e.g., volume fractions) using a regression analysis. This is beyond the scope of this paper and is subjected to future investigation.

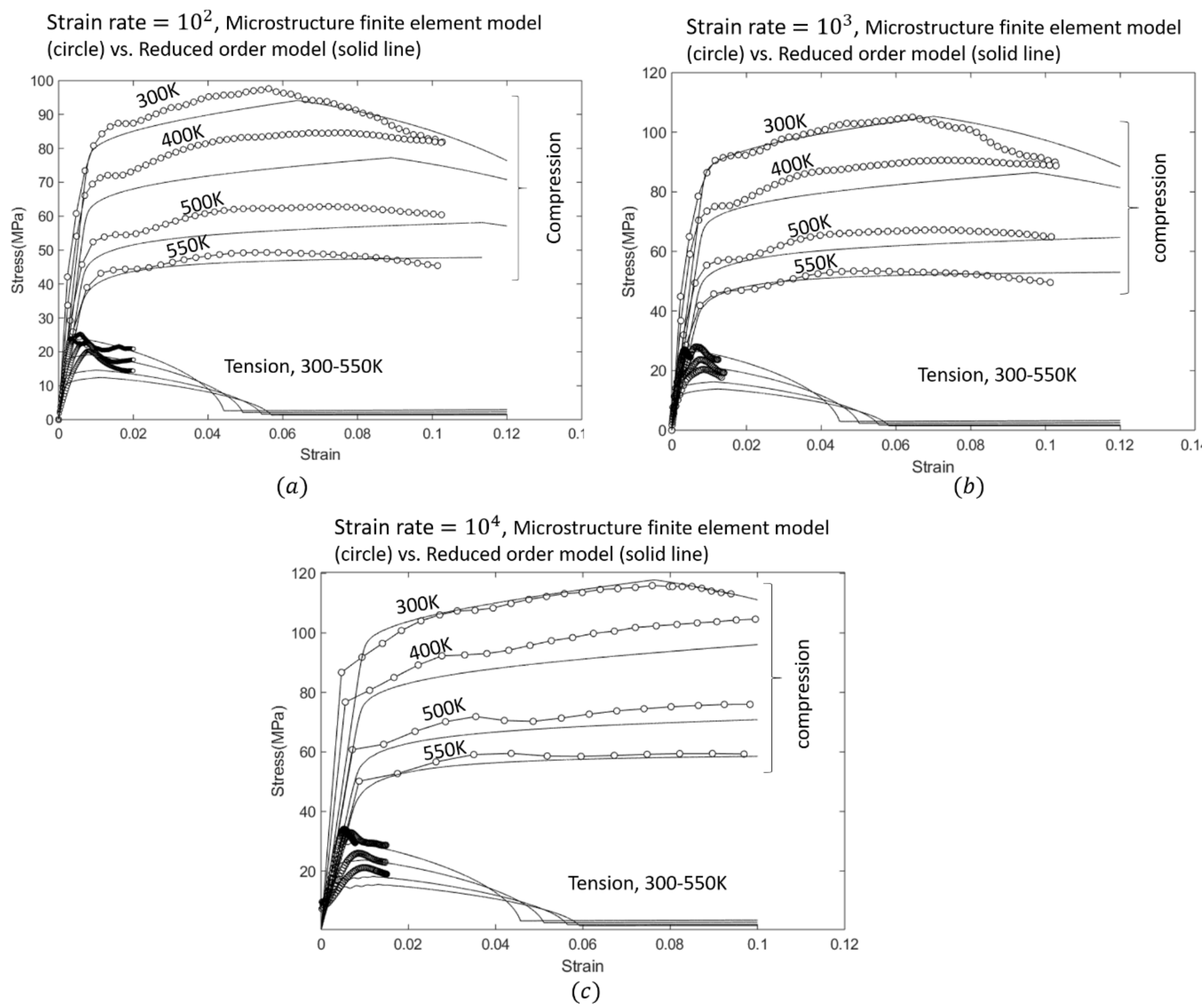

Figure 4. Generating stress-strain data using the calibrated micro-RVE model across a range of strain rates and temperatures, and macro-ROM calculation results to fit the virtually generated data.

3.2 Scratch test simulations

In order to test the reduced order model's accuracy and capability at relevant 'rub' conditions, a scratch experiment of Metco601 is conducted for comparison to simualtion. The scratch test invokes a very complicated stress state and tribological conditions similar to rub but is much less costly than actual rub test, therefore serves as a benchmark test for model validation.

The scratch test is conducted using a Rockwell C diamond scratch tip which has a 120 degree conical shape with a 200 um radius tip geometry, as illustrated in Fig. 5a. A linearly increasing load at 10N/s rate and max load of 150N is applied in vertical direction, while the scratch tip moves in transverse direction at a constant velocity of 0.1667mm/s. The total plunge depth (into the coating) is about 3 mm and total sliding distance is up to 2 mm. The scratch test simulation using the Reduced order model is illustrated in Fig. 5b. The setup of the model follows the same condition as in the experiment. The indenter tip which is made of diamond is modeled as rigid C3D8T elements, while a $14mmL \times 7.4mmW \times 3.9mmH$ size Metco601 abradable part, meshed into 240371 C3D8T elements, is subjected to the interaction with the scratch tip. The abradable is fixed for displacement at the nodes on bottom and transverse surfaces during the simulation. Fig. 5b shows the stress distribution after 0.8mm plunge depth into the Metco601 coating, and the corresponding load-displacement curves is compared with experiments in Fig.5c. The predicted loads in both the sliding and plunging directions match the experimental results, providing confidence in the reduced order model.

Table 1. Constitutive model parameters for micro-RVE model

AlSi phase	A	B	C	n	m	d_1^{AlSi}	d_2^{AlSi}
	225MPa	185MPa	0.018	0.28	1.43	0.037	5.5
	d_3^{AlSi}	d_4^{AlSi}	E^D				
	0.147	6.8	500 J/mm^3				
PES phase	θ_g^{ref}	β^{beta}	c^{poly}	θ_f^{ref}	E_1	E_2	E_3
	545.22K	8×10^{-5}	$1500J/kg/K$	650.0K	10.5GPa	1.35GPa	10MPa
	m_1	m_2	m_3	s	$\dot{\gamma}_0$	ΔH_β	τ_{int}^{ref}
	0.5	40.0	20.0	0.26	1.16/s	30kJ/mol	100MPa
	V	c_1^g	c_2^g	τ_{ps}/τ_{int}	h	$\widehat{m}$	α_p
	$9.75 \times 10^{-29} m^3$	32.58	83.5	0.6	$60MPa$	0.165MPa	0.26
	$C_R(0)$	$N(0)$	a	b	σ_{poly}^{crit}	d_{poly}^{hy}	
	91.15MPa	1.515	0.155MPa	0.0025	42MPa	0.1MPa/K	
Inter-face	E^{coh}	$\delta_{n/t/s}^0$	$\delta_{n/t/s}^f$				
	10GPa	$0.001\mu m$	$0.001\mu m$				

Table 2. Constitutive model parameters for macro-ROM

k	a	$\hat{g}_0$	$\dot{d}_0$	m	$\hat{\alpha}$	$\hat{\beta}$
-0.45	1	8.2MPa	0.006	0.045	8MPa	0.13
s_β	ψ	$\widehat{H}$	s_H	s_{g_0}	d_1^{ROM}	d_2^{ROM}
-0.0002/K	0.5	-30MPa	79MPa	-0.066MPa/K	0.024	5.0
d_3^{ROM}	d_4^{ROM}	d_5^{ROM}	d_1^{degrad}	d_2^{degrad}	d_3^{degrad}	d_4^{degrad}
0.053	3.0	0.001	0.035	3.5	0.5	0.2

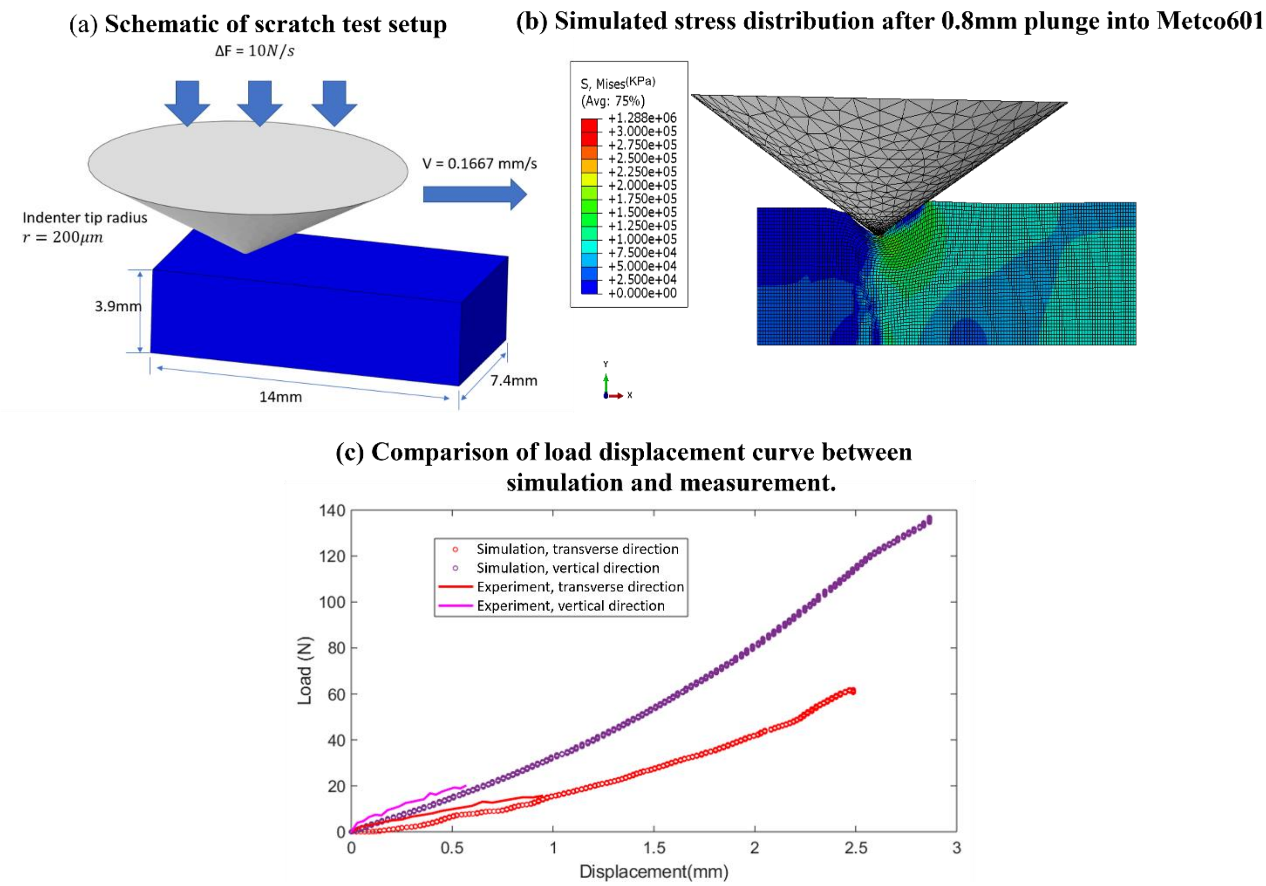

Figure 5. (a) Illustration of the scratch test model (b) Distribution of von Mises stress in the METCO601 coating during scratch test after a plunge depth of 0.8mm. (c) the load-displacement curve in both vertical direction and transverse direction, with both experiments and simulation results.

Conclusion

In sum, this research provides a micro-macro modeling strategy to predict the complex mechanical behavior associated with the microstructure of the thermally sprayed AlSi-PES abradable seal coatings materials. The model framework transfers the micro-RVE model's intrinsic features to the fast and high-fidelity component scales simulations for investigating the 'rub' events. Especially, this work has achieved the following results:

1. The micro-representative volume element (RVE) is virtual reconstructed from the xCT reconstruction of the Metco 601 microstructure.
2. The constitutive model including damage laws for the AlSi phase, the polyester phase, and their interface have been established respectively, and calibrated and validated with SHPB tensile and compressive test results at various strain rates and temperature conditions.
3. The micro-model successfully captured the experimentally observed strong tension-compression asymmetry due to interface debonding, further proves the models' reliability.
4. A large number of simulations were conducted using the micro-model to generate data for more temperature and strain rate range related to 'rub' physical process.
5. The macroscopic reduced order (macro-ROM) constitutive model is proposed with features of the tension-compression asymmetric, as well as the rate and temperature-sensitive plasticity and damage laws. The macro model is calibrated and validated using the virtually generated test dataset.
6. Due to the turbine blade-abradable coating-housing 'rub' simulation is proprietary, a scratch test simulation is utilized to validate the macro-ROM model, which is essentially similar to turbine rub condition. The results show the reliability of the reduced order model for component scale 'rub'-like simulation.

The combination of the micro-RVE model and macro-ROM model is expected to improve the current abradable rub modeling accuracy by introducing more reliable, microstructure-derived material behavior model. The micro-macro framework provides numerical tool for guiding abradable material improvement and innovation. However, despite the excellent matching between the simulation and the experiment results, this work still has the shortcomings. Performing high velocity shear tests of the Metco601 abradable is very challenging and the model is therefore only validated with tension and compression conditions, resulting to somewhat insufficient data for validating the material behavior. The virtual dataset generated using micro-model also did not consider bi-axial and tri-axial loading, which needs to be improved. The future expansion of this work will merit further investigation of this model in other conditions as well as extension of this approach to other abradable material systems.

Acknowledgement

This research was sponsored by the Oak Ridge National Laboratory (ORNL), Energy and Transportation Science Division. ORNL is managed by UT-Battelle, LLC for the U.S. Department of Energy under Contract DE-AC05 00OR22725. This work was funded by the HPC4materials program supported by U.S. Department of Energy Office of Fossil Energy in collaboration with Raytheon Technologies Corporation - Pratt & Whitney Division. Computing support by the Compute and Data Environment for Science (CADES) at Oak Ridge National Laboratory is gratefully acknowledged.

Author contributions: Jiahao Cheng: Writing – original draft, Investigation, Formal Analysis; Xiaohua Hu: Writing – review & editing, Investigation, Supervision, Funding acquisition, Project administration; William Joost: Writing – review & editing, Investigation, Supervision, Funding acquisition, Project administration, Validation; Xin Sun: Writing – review & editing, Conceptualization, Supervision, Funding acquisition.

Conflicts of interest or competing interests: The authors certify that they have NO affiliations with or involvement in any organization or entity with any financial interest (such as honoraria; educational grants; participation in speakers' bureaus; membership, employment, consultancies, stock ownership, or other equity interest; and expert testimony or patent-licensing arrangements), or non-financial interest (such as personal or professional relationships, affiliations, knowledge or beliefs) in the subject matter or materials discussed in this manuscript.

Data and code availability: N/A.

Supplementary information: N/A.

Ethical approval: There is no experiments carried out in this work that involve human tissues.

Reference:

Almeida, P., Gibert, C., Thouverez, F., & Ousty, J. P. (2015). Numerical analysis of bladed disk - Casing contact with friction and wear. *Proceedings of the ASME Turbo Expo*, *7B*. https://doi.org/10.1115/GT2015-43435

Arruda, E. M., & Boyce, M. C. (1993). Evolution of plastic anisotropy in amorphous polymers during finite straining. *International Journal of Plasticity*. https://doi.org/10.1016/0749-6419(93)90034-N

Bakker, K. (1997). Using the finite element method to compute the influence of complex porosity and inclusion structures on the thermal and electrical conductivity. *International Journal of Heat and Mass Transfer*, *40*(15), 3503–3511. https://doi.org/10.1016/S0017-9310(97)00017-3

Batailly, A., Legrand, M., Millecamps, A., Garcin, F., Batailly, A., Legrand, M., Millecamps, A., Numerical-experimental, F. G., & Legrand, M. (2012). *Numerical-experimental comparison in the simulation of rotor / stator interaction through blade-tip / abradable coating contact To cite this version : HAL Id : hal-00746632*. 0–20.

Berthoul, B., Batailly, A., Stainier, L., Legrand, M., & Cartraud, P. (2018). Phenomenological modeling of abradable wear in turbomachines. *Mechanical Systems and Signal Processing*, *98*, 770–785. https://doi.org/10.1016/j.ymssp.2017.05.020

Bolot, R., Aussavy, D., & Montavon, G. (2017). Application of FEM to estimate thermo-mechanical properties of plasma sprayed composite coatings. *Coatings*, *7*(7), 1–12. https://doi.org/10.3390/coatings7070091

Bolot, R., Seichepine, J. L., Qiao, J. H., & Coddet, C. (2011). Predicting the thermal conductivity of AlSi/polyester abradable coatings: Effects of the numerical method. *Journal of Thermal Spray Technology*, *20*(1–2), 39–47. https://doi.org/10.1007/s11666-010-9592-y

Cao, D. (2023a). Enhanced buckling strength of the thin-walled continuous carbon fiber–reinforced thermoplastic composite through dual coaxial nozzles material extrusion process. *International Journal of Advanced Manufacturing Technology*, *128*(3–4).

https://doi.org/10.1007/s00170-023-12014-8

Cao, D. (2023b). Strengthening the interphase of thermoplastic sandwich composites by interleaving carbon nanotube yarns. *Materials Today Communications*, *36*. https://doi.org/10.1016/j.mtcomm.2023.106655

Cao, D., Bouzolin, D., Lu, H., & Griffith, D. T. (2023). Bending and shear improvements in 3D-printed core sandwich composites through modification of resin uptake in the skin/core interphase region. *Composites Part B: Engineering*, *264*. https://doi.org/10.1016/j.compositesb.2023.110912

Cheng, J., Gussev, M., Allen, J., Hu, X., Moustafa, A. R., Splitter, D. A., & Shyam, A. (2020). Deformation and failure of PrintCast A356/316 L composites: Digital image correlation and finite element modeling. *Materials and Design*, *195*, 109061. https://doi.org/10.1016/j.matdes.2020.109061

Cheng, J., Hu, X., Lancaster, D., Sun, X., & Joost, W. (2022). Modeling deformation and failure in AlSi-polyester abradable sealcoating material using microstructure-based finite element simulation. *Materials and Design*, *219*. https://doi.org/10.1016/j.matdes.2022.110791

Duramou, Y., Bolot, R., Seichepine, J. L., Danlos, Y., Bertrand, P., Montavon, G., & Selezneff, S. (2014). Relationships between microstructural and mechanical properties of plasma sprayed AlSi-polyester composite coatings: Application to abradable materials. *Key Engineering Materials*, *606*. https://doi.org/10.4028/www.scientific.net/KEM.606.155

Faraoun, H. I., Seichepine, J. L., Coddet, C., Aourag, H., Zwick, J., Hopkins, N., Sporer, D., & Hertter, M. (2006). Modelling route for abradable coatings. *Surface and Coatings Technology*, *200*(22-23 SPEC. ISS.). https://doi.org/10.1016/j.surfcoat.2005.11.105

Hesebeck, O. (2015). Consideration of the restriction of lateral contraction in the elastic behaviour of cohesive zone models. *International Journal of Adhesion and Adhesives*, *62*, 165–171. https://doi.org/10.1016/j.ijadhadh.2015.07.003

Jadhav, A. D., Padture, N. P., Jordan, E. H., Gell, M., Miranzo, P., & Fuller, E. R. (2006). Low-thermal-conductivity plasma-sprayed thermal barrier coatings with engineered microstructures. *Acta Materialia*, *54*(12), 3343–3349. https://doi.org/10.1016/j.actamat.2006.03.024

Kotzé, J. P., Von Backström, T. W., & Erens, P. J. (2013). High temperature thermal energy storage utilizing metallic phase change materials and metallic heat transfer fluids. *Journal of Solar Energy Engineering, Transactions of the ASME*, *135*(3). https://doi.org/10.1115/1.4023485

Kulkarni, A., Wang, Z., Nakamura, T., Sampath, S., Goland, A., Herman, H., Allen, J., Ilavsky, J., Long, G., Frahm, J., & Steinbrech, R. W. (2003). Comprehensive microstructural characterization and predictive property modeling of plasma-sprayed zirconia coatings. *Acta Materialia*, *51*(9), 2457–2475. https://doi.org/10.1016/S1359-6454(03)00030-2

Legrand, M., & Pierre, C. (2009). Detc2009-87669 Numerical Investigation of Abradable Coating Wear Through. *Engineering Conference*, 1–10.

Lye, R., Bennett, C., Rouse, J., & Zumpano, G. (2022). An inverse analysis method for determining abradable constitutive properties. *Materials Today Communications*, *33*. https://doi.org/10.1016/j.mtcomm.2022.104571

Michlik, P., & Berndt, C. (2006). Image-based extended finite element modeling of thermal barrier coatings. *Surface and Coatings Technology*, *201*(6), 2369–2380. https://doi.org/10.1016/j.surfcoat.2006.04.003

Nyssen, F., & Batailly, A. (2019). Thermo-Mechanical Modeling of Abradable Coating Wear in Aircraft Engines. *Journal of Engineering for Gas Turbines and Power*, *141*(2), 1–11. https://doi.org/10.1115/1.4041647

Olgac, N., Zalluhoglu, U., & Kammer, A. S. (2014). On blade/casing rub problems in turbomachinery: An efficient delayed differential equation approach. *Journal of Sound and Vibration*, *333*(24), 6662–6675. https://doi.org/10.1016/j.jsv.2014.06.038

Pellegrino, A., Jesus, P. M. M., Dragnevski, K., Zumpano, G., & Petrinic, N. (2018). Temperature and strain rate dependent mechanical response of METCO 601 aluminium-polyester abradable seal coating. *EPJ Web of Conferences*, *183*, 04012. https://doi.org/10.1051/epjconf/201818304012

Ribesse, A., Favache, A., Lemoine, G., Bailly, C., Jacques, P., & Pardoen, T. (2014). Multiscale mechanical and tribological characterization of alsi abradable material. *7th International Conference on Fracture of Polymers, Composites and Adhesives*.

http://hdl.handle.net/2078.1/173390

Rice, J. R., & Tracey, D. M. (1971). *and Concepts That Can Provide the Stiffness and Strength Needed To . Primary Design Function, But That Will Efficiently and Progressively With Fracture During Crash Loading. 678*(January).

Richeton, J., Ahzi, S., Vecchio, K. S., Jiang, F. C., & Makradi, A. (2007). Modeling and validation of the large deformation inelastic response of amorphous polymers over a wide range of temperatures and strain rates. *International Journal of Solids and Structures*, *44*(24), 7938–7954. https://doi.org/10.1016/j.ijsolstr.2007.05.018

Richeton, J., Schlatter, G., Vecchio, K. S., Rémond, Y., & Ahzi, S. (2005). A unified model for stiffness modulus of amorphous polymers across transition temperatures and strain rates. *Polymer*. https://doi.org/10.1016/j.polymer.2005.06.103

Salvat, N., Batailly, A., & Legrand, M. (2013). Modeling of abradable coating removal in aircraft engines through delay differential equations. *Proceedings of the ASME Turbo Expo*, *7 B*, 0–17. https://doi.org/10.1115/GT2013-94400

Skiba, S., Chevrier, B., Faure, L., & Philippon, S. (2021). Thermoelastoviscoplastic Bilinear Compressive Constitutive Law of an AlSi-PE Abradable Material Based on Experimental Investigations. *Journal of Dynamic Behavior of Materials*, *7*(3). https://doi.org/10.1007/s40870-021-00294-8

Skiba, S., Faure, L., Philippon, S., & Papasidero, J. (2020). Experimental Investigation of the Mechanical Behavior of an AlSi-PE Abradable Coating at High Strain Rates for a Large Range of Temperatures. *Journal of Dynamic Behavior of Materials*, *6*(2). https://doi.org/10.1007/s40870-020-00242-y

Wang, Z., Kulkarni, A., Deshpande, S., Nakamura, T., & Herman, H. (2003). Effects of pores and interfaces on effective properties of plasma sprayed zirconia coatings. *Acta Materialia*, *51*(18), 5319–5334. https://doi.org/10.1016/S1359-6454(03)00390-2

Williams, R. J. (2011). *Resulting From Heavy Tip Rubs Using an Implicit Time Marching*. 1–10.